View Article Online / Journal Homepage / Table of Contents for this issue

Journal of Materials Chemistry

www.rsc.org/materials

Volume 20 | Number 19 | 21 May 2010 | Pages 3777–3996

Open Access Article. Published on 13 April 2010. Downloaded on 7/19/2025 5:50:03 AM.

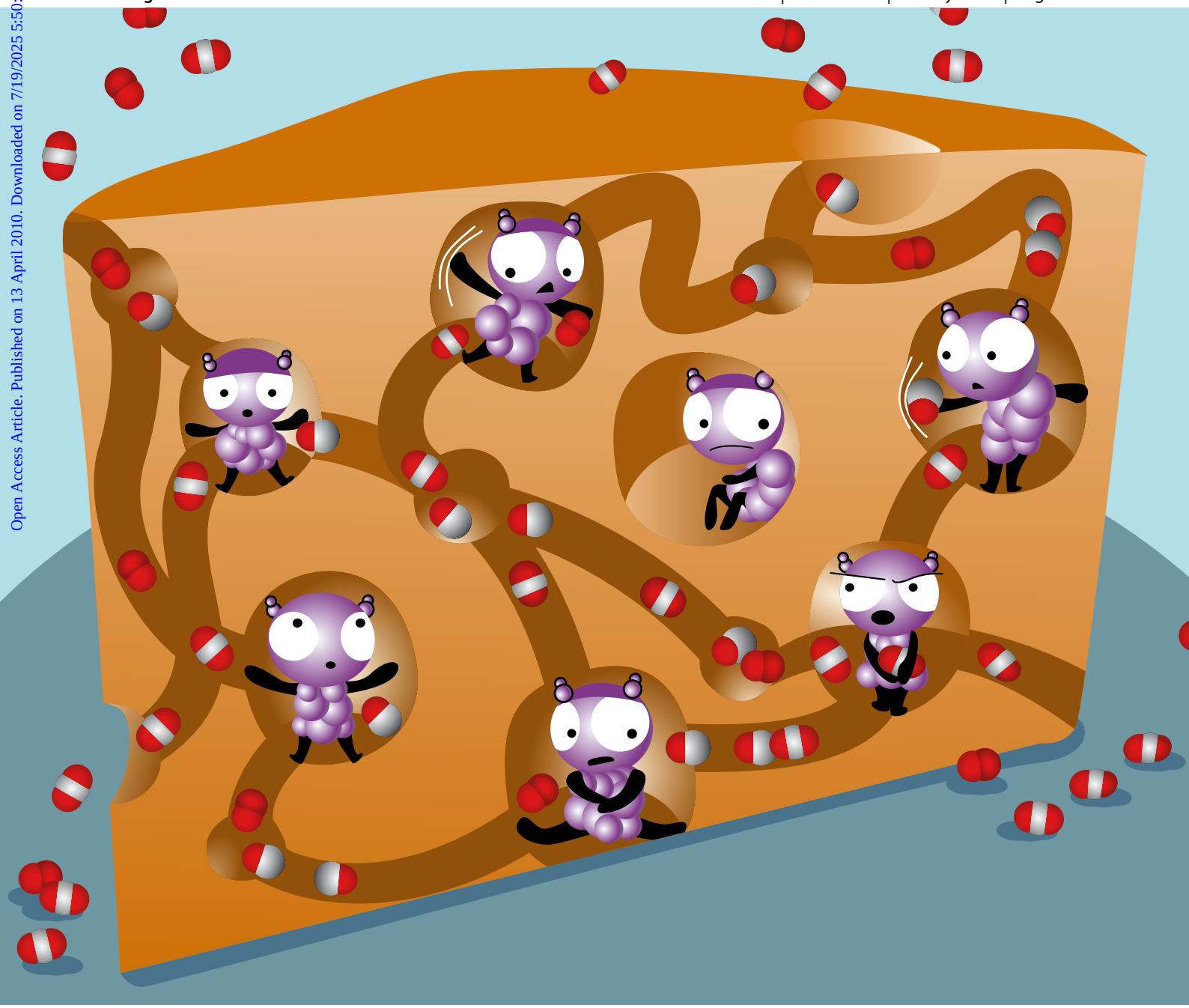

ISSN 0959-9428

PAPER
G. Rothenberg *et al.*
Preventing sintering of Au and Ag nanoparticles in silica-based hybrid gels using phenyl group spacers

FEATURE ARTICLE
A. Tarancón *et al.*
Advances in layered oxide cathodes for intermediate temperature solid oxide fuel cells

RSC Publishing

0959-9428(2010)20:19;1-L

View Article Online

Preventing sintering of Au and Ag nanoparticles in silica-based hybrid gels using phenyl spacer groups†

Nina M. Wichner,[a] Jurriaan Beckers,[b] Gadi Rothenberg*[b] and Hubert Koller*[a]

Received 6th January 2010, Accepted 12th March 2010
First published as an Advance Article on the web 13th April 2010
DOI: 10.1039/c000105h

Open Access Article. Published on 13 April 2010. Downloaded on 7/19/2025 5:50:03 AM.

Gold and silver metal salts were reduced in the presence of phenylethylthiol as capping agent to form metal nanoparticles of 2.1–2.4 nm diameter. These clusters were then added to a sol–gel process using phenyltriethoxysilane as a hybrid component to optimize the dispersion of the metal particles in the matrix. The encapsulated metal particles grow in the sol–gel process to an average diameter of 6 nm. This method permits a controlled variation of the materials' porosity by simply regulating the synthesis pH values. Optimized mixed micro-/mesoporous materials are obtained at pH = 6. The metal particles and the matrix are thermally stable, and catalyze CO oxidation.

Introduction

Research in modern sol–gel science attempts making new materials by rational design of the molecular environment.[1,2] There is a large range of applications for hybrid sol–gel materials, including selective adsorption and catalysis with tailor-made porosity.[3–5] Although the idea of molecular imprinting of silica gels dates back to Pauling's dye experiments,[6] further exploitation started much later, with imprinted cross-linked polymers.[7] Today, designing porous solids with well defined parameters (shape, size, polarity, site accessibility) still remains a challenge, *e.g.* when catalytically active metal particles with controlled dispersion have to be deposited on the solid support. Porous properties are of utmost importance in catalysis and separation science.[8–12] In most classical work in this area, the metal particles are generated on a preformed support. Only more recent studies show the *in situ* incorporation of well defined metal nanoclusters in sol–gel materials.[13,14]

In heterogeneous catalysis, one of the thorniest problems is preventing catalyst sintering.[15,16] This is especially true for redox reactions, where the catalytically active metal particles often switch between oxides and zerovalent metals.[17,18] The catalytic activity of gold metal clusters, for instance, decreases sharply above 5 nm diameter. Indeed, until the 1990s, when methods were developed for preparing small gold clusters, the metal was deemed catalytically inactive.[13,19,20] The encapsulation of stable metal nanoparticles (Au, Ag, Pt) in ordered mesoporous SBA-15 silicas was reported by Somorjai and co-workers.[21] They used a triblock copolymer to stabilize the metal nanoparticles as well as to template the periodic mesoporous silica structure. After calcination, the metal clusters reside in the channels of the mesoporous host matrix.[14,22] Avnir *et al.* achieved the entrapment of several types of semiconductor nanocrystals in polystyrene/silica composite spherical particles.[23] Imprinting of silica with Au nanoparticles using aminosilanes was achieved at high loadings,[24,25] and phenyl-functionalized silica gels with embedded gold particles were also prepared in a basic medium, albeit with particle sizes larger than 10 nm.[26]

We describe here the encapsulation of noble metal nanoclusters during the growth of an organic–inorganic hybrid gel. The gel matrix protects the metal particles from sintering, while allowing sufficient reactant/product accessibility for catalysis. Our approach differs from other published procedures in that the metal nanoparticles are prepared first, and they are then encapsulated with polymerizable T building units, R-Si(OR′)$_3$, with an R group that favors selective assembly with the particle shell surface.

A variety of sol–gel encapsulation strategies are used for preparing materials with controlled porosity and surface chemistry. The covalent approach to capture specific species linked by chemical bonds in a sol–gel network is well understood. However, non-covalent encapsulation of a template (so-called 'structure directing agent' in crystalline materials or 'porogenic agent' in amorphous ones) requires an understanding of the underlying intermolecular interactions. Previously, we reported the sol–gel encapsulation of pharmaceutical drug molecules with the aim to control the release kinetics by the use of silica and organically modified silica gels.[27] The release kinetics of drugs containing aromatic groups from phenyl-functionalized hybrid gels was relatively slow, indicating a firm encapsulation due to interactions between aromatic groups. Tsuzuki *et al.* studied the interaction strength between simple aromatic systems.[28,29] Such interaction energies can be on the order of −10 to −20 kJ mol^{-1} according to their theoretical calculations.

We show here that a firm encapsulation of the metal nanoparticles is possible, making them sinter-resistant for catalytic applications. As we previously reported, the pore structure can be varied during the sol–gel encapsulation of drugs. Under acidic sol–gel conditions, the surface charge of the silica correlates with the porosity. A simple model suggests that encapsulation of charge compensating cations is required, when the surface is

[a]*Institut für Physikalische Chemie, Westfälische Wilhelms-Universität, Corrensstrasse 28/30, 48149 Münster, Germany. E-mail: hubert.koller@uni-muenster.de; Fax: +49 251 8323409*
[b]*Van't Hoff Institute for Molecular Sciences, University of Amsterdam, Nieuwe Achtergracht 166, 1018 WV Amsterdam, The Netherlands. E-mail: g.rothenberg@uva.nl; Fax: +31 (0)20 525 5604*

† Electronic supplementary information (ESI) available: N_2 adsorption after HNO_3 treatment, N_2 adsorption after temperature and redox treatment cycles, Raman spectra. See DOI: 10.1039/c000105h

 This journal is © The Royal Society of Chemistry 2010

View Article Online

Open Access Article. Published on 13 April 2010. Downloaded on 7/19/2025 5:50:03 AM.

negatively charged at pH values above 2–3. Hydrated cations (*e.g.* H_3O^+) are the porogenic agents. At the isoelectric point (pH = 1–3, depending on the composition) no porosity forms.[30,31] Therefore, two effects must be balanced: the ionic surface interactions of the sol–gel materials and the hydrophobic interactions between phenyl groups. Here we will show that controlling the synthesis pH allows the adjusting of the porosity.

Experimental

Materials

The nanoparticles were synthesized *via* the Brust reaction.[32–34] $HAuCl_4$ (0.84 mmol) was dissolved in water (0.55 mol) and was phase-transferred into toluene with tetraoctylammonium bromide (0.5 mmol), followed by addition of phenylethylthiol (2.4 mmol, a 3-fold molar excess relative to the metal). This mixture was cooled in an ice bath for 30 minutes. Then, the metal was reduced by $NaBH_4$ (8.3 mmol in 0.28 mmol water) at 273 K, with formation of H_2 gas. The formation of the arenethiolate monolayer-protected metal clusters (Au and Ag) was evidenced by an immediate darkening of the toluene phase. The suspension was stirred in an ice bath for 24 h, after which the two phases were separated, and the product, $Au_{x1}(SC_2H_4Ph)_{y1}$, was isolated from the toluene phase. The Ag nanoparticles were similarly prepared, starting from $AgNO_3$, as previously reported by Oliveira *et al.*,[35] with no indications for the precipitation of AgBr observed by XPS.

In a typical sol–gel reaction, phenyltriethoxysilane (PhTS, 4.56 mmol), and water (0.09 mol) were mixed with THF (0.06 mol). The mixture was acidified to pH = 1.2 (0.05 mL conc. HNO_3, Aldrich) for the silver samples and the metal-free sample or 0.05 mL conc. HCl (AppliChem) for the gold samples. The addition of the acid was carried out quickly within the time-scale of a second. After 1 h stirring, the phenylethylthiol-coated metal nanoparticles, dissolved in 0.06 mol THF, were added. The suspension was stirred for another hour, and then 0.0223 mol tetramethoxysilane (TMOS) was added. The pH was then increased after 3 h with NH_3(aq) to its final value. Gelation occurred after 2–20 min, depending on the pH value. The compositions and sample notations are listed in the ESI†. Finally, the organic components were then removed from the products by calcination at a final temperature of 873 K in air. For calcination, the temperature was increased from room temperature to 373 K with a heating rate of 1 K min^{-1}. Then, after two hours, the temperature was increased with a rate of 2 K min^{-1} to 873 K, and held for 6 h.

Sample I is a hybrid gel made at pH = 7 which was post-synthetically impregnated with Ag NPs. The particles were dissolved in THF, and the solution was combined with the solid gel after which the THF was evaporated. The Ag/Si ratio was 0.016.

Instrumentation

N_2 adsorption was measured on a Micromeritics ASAP 2010 apparatus at 77 K. Before the measurements the silicates were evacuated at 373 K. Pore diameters were determined using the BJH method on the desorption experiment. The *t*-plot method was applied to separate micro-/mesoporosity from the external surface adsorption. Metal particle sizes were determined by transmission electron microscopy (TEM, Hitachi H800 NA, operating at 200 kV). The dried gel samples were dispersed in ethanol, and then a droplet was placed on the Cu grid and then dried for TEM analyses.

Powder X-ray diffraction was performed with CuKα radiation using a Guinier camera. α-Quartz was used as an internal standard. The powder patterns were analyzed by using the program WINXPOW.

Thermogravimetric and differential thermal analyses were performed in Netzsch STA 409 C thermal analyzer. About 40 mg of sample were heated at a rate of 10 K min^{-1} between 298 K and 1173 K in an oxygen flow. The base line correction was made using Al_2O_3 as the reference sample.

Temperature programmed reduction (TPR) measurements were performed on a homemade system. Typically, around 100 mg of the sample are taken for a TPR measurement. Before the reduction, the samples are oxidized in a 50 mL min^{-1} flow of 5% v/v O_2 in Ar mixture up to 573 K. After cooling to room temperature, the sample was flushed by a 20 mL min^{-1} flow of 67% v/v H_2 in Ar mixture. After 5 minutes the two filaments were heated to 423 K. One of the two filaments was placed in the measurement chamber together with the sample, and filament 2 was used as the reference. The difference in the filament temperatures was determined based on their electric resistance. The signal is produced due to the consumption of hydrogen in the sample which causes a different heat transport by H_2 in the sample chamber and the reference. The TPR scan was carried out from ambient temperature to 623 K with a heating rate of 10 K min^{-1}.

Catalytic CO oxidation

Prior to the catalytic tests, the samples were calcined *in situ* to 573 K (30 min hold) in 5% v/v O_2/He. In a typical reaction, 50 mg of catalyst were placed on a quartz wool plug in a 4 mm quarts reactor. A 50 mL min^{-1} flow of 2% v/v CO and 2% v/v O_2 in He, with 1% v/v Ar added as internal standard, was fed over the catalyst, which was heated from room temperature to 873 K in 50 K steps (heating rate: 5 K min^{-1}). The exit gas of each reactor was analyzed by mass spectrometry at each temperature using a Balzers Prisma QME200 spectrometer, equipped with a Channeltron® detector.

Results and discussion

Scheme 1 summarizes the synthetic procedure for the nanoparticle (NP) encapsulation. The Au or Ag NPs are capped with phenylethylthiol which may form non-covalent interactions with phenyltriethoxysilane. Sol–gel polymerization with tetramethoxysilane and phenyltriethoxysilane is carried out under acidic conditions. Fast hydrolysis of the precursors, PhTS and TMOS, takes place at the first pH step (pH = 1.2). At this low pH value, the condensation is slow and separation of the two hybrid precursors into different solid phases is impeded. These clear solutions are then treated with aqueous NH_3, thus increasing the pH of the mixture to the final target value, where condensation is accelerated.[27,36,37] The organic components, *i.e.* the capping agent of the NPs and the matrix phenyl groups, are removed by calcining the solids after the sol–gel reaction.

View Article Online

Open Access Article. Published on 13 April 2010. Downloaded on 7/19/2025 5:50:03 AM.

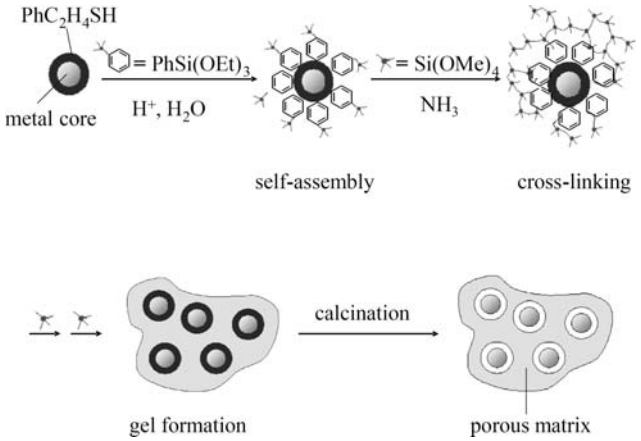

Scheme 1 Reaction scheme for the encapsulation of metal clusters in a porous silica matrix.

Fig. 1 shows the X-ray powder diffraction pattern of uncalcined samples. The as-made Au^0 and Ag^0 NPs before sol–gel encapsulation, $Au_x(SC_2H_4Ph)_y$ and $Ag_x(SC_2H_4Ph)_y$, show Bragg reflections that differ from the X-ray powder pattern of the bare metals. Analysis of the Bragg pattern yields a cubic primitive lattice with a lattice constant of 2.1–2.4 nm. As a consequence, from the cubic primitive packing of the NPs it can be concluded that their size is of the same values. This lattice distance is well within the expected size of the nanoparticles for such types of reactions. Note that the Bragg peaks at very low diffraction angles are outside the experimentally available diffraction window. The Ag NPs encapsulated in the sol–gel matrix are shown with three different loadings. While the sample with the highest loading with a Ag/Si ratio of 0.033 shows some XRD peaks of the pure NPs due to phase separation from the amorphous gel, the other two samples are almost amorphous, except for a small peak of the most intense reflection at 4.8°. Similar observations are made for the gold samples. The gel with the lower loading of Au/Si = 0.012 is almost amorphous, except for a small reflection of Au(111), and the sample with higher loading (Au/Si = 0.035) shows phase separation of the pure NPs. These observations show that the NPs can be dispersed in the sol–gel matrix up to a threshold concentration above which phase separation of the pure NPs occurs. The observation of an XRD peak, Au(111), of metallic gold occurs only for the gel made at pH = 7. As will be shown below, mesopores are formed at this pH value, whereas the gel matrices are microporous at lower pH values. Obviously, gold has a tendency to form larger metallic particles which become visible in XRD, when the surrounding matrix permits such growth because large pores exist. Silver, on the other hand, does not show such a growth of the particle size.

The XRD powder patterns after calcination are shown in Fig. 2. The gold samples all show Bragg peaks of metallic gold, and the silver samples show a very broad and weak peak of silver oxides between 30–32° 2Θ. The broader signal centered at ~21° originates from the amorphous silica. The sharp reflections for gold are assigned to a small number of large gold particles which are present in samples A and C. On the other hand, the silver samples do not show such large particles, and the broad peak originates from a distribution of small particle sizes. Silver oxide is unexpected to exist at calcination temperatures of 873 K, as disproportionation to Ag^0 and O_2 would normally occur. The existence of silver oxide in the sample may be due to the small size of the particles, as indicated by the broad XRD peak. The Au samples do not show any indication of oxide formation. This is probably due to the higher redox potential of gold, and the larger particle sizes, as suggested based on the relatively narrow XRD peaks.

Fig. 3 shows representative thermoanalyses for the Au sample C (Au/Si = 0.035), the silver sample D (Ag/Si = 0.033), and a metal-free hybrid gel, G. All three samples were prepared at pH = 6. The three graphs in the figure show the weight loss (Fig. 3a: TG = thermogravimetry) the differential thermogravimetry,

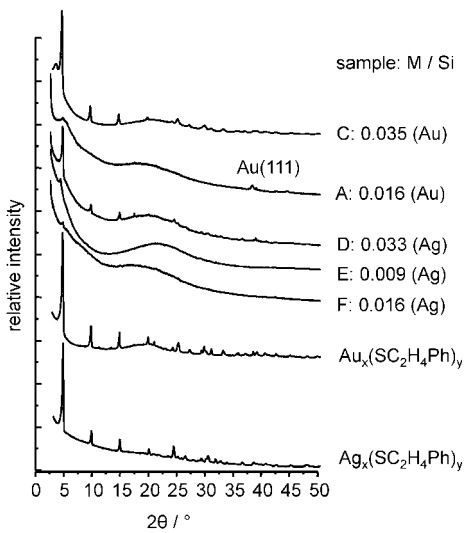

Fig. 1 XRD patterns of gold and silver particles stabilized by phenylethylthiol and with different loadings.

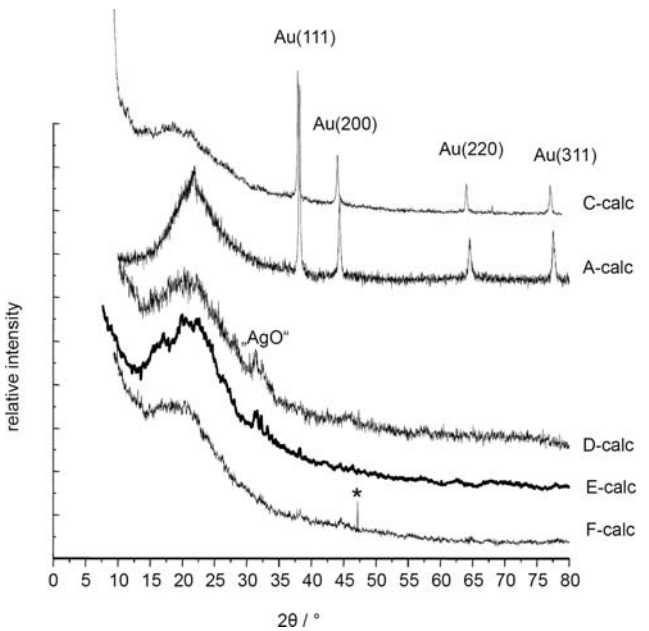

Fig. 2 XRD patterns after calcination at 873 K (* indicates a background signal).

This journal is © The Royal Society of Chemistry 2010

View Article Online

Open Access Article. Published on 13 April 2010. Downloaded on 7/19/2025 5:50:03 AM.

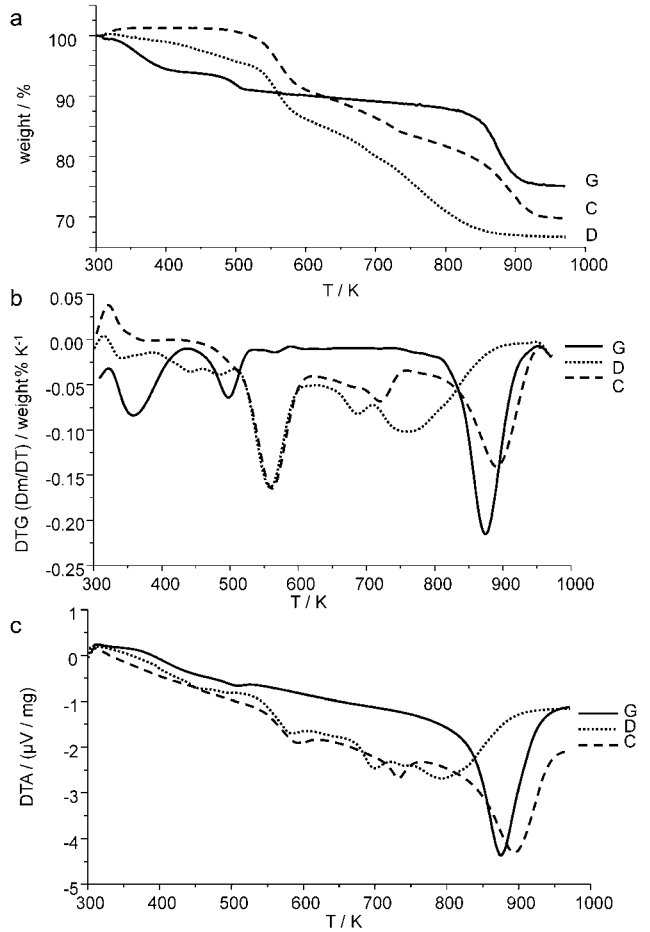

Fig. 3 Thermoanalytic data of the gold sample with Au/Si = 0.035, C, the silver sample with Ag/Si = 0.033, D, and the metal free sample, G; (a) thermogravimetry (TG), (b) differential thermogravimetry (DTG), and (c) differential thermal analysis (DTA).

DTG (Fig. 3b), and the differential thermal analysis, DTA (Fig. 3c). We discuss the DTG curves here which are derived from the TG experiment, because they allow for a better separation of the temperature steps of the different events permitting a more accurate analysis of the quantitative weight loss. The metal free hybrid gel, G, shows some weight loss at 500 K and below, and a large event between 840 and 900 K. The latter is assigned to the combustion of the phenyl groups (15%), whereas the low-temperature loss is most likely due to water, either physisorbed or generated by silanol condensation. Three thermal events are identified for sample C: event I, between 500 and 620 K, originates from the loss of capping agent of the Au NPs (11%). The weight loss is in excellent agreement with the expected value. Event II, between 690 and 760 K (4%), is most likely due to the condensation of silanol groups and subsequent loss of water. The last event III at 890 K is due to the combustion of the matrix phenyl groups (16%). The Au sample does not show a significant weight loss from physisorbed water below 600 K which is due to the hydrophobic properties of the sample. Although the weight loss is completed at 923 K in the thermogravimetric analysis, the calcination of the sample at 873 K for 6 h is sufficient to yield a product that is free of any organic residues, as no phenyl group vibrations are detected by Raman spectroscopy (see ESI†). The calcination experiment is carried out for a longer time at the maximum temperature compared to the thermoanalysis in which the temperature is varied slowly. The silver sample, D, shows a similar behavior as the Au sample for the loss of capping agent at 560 K (10%). Event II at 680 K also occurs with a water loss of 5%. Interestingly, the combustion of the matrix phenyl groups, event III, is shifted to considerably lower temperatures compared to the Au sample or the bare hybrid gel. The maximum occurs here at 770 K, and the DTG peak is much broader than for samples C and G. The DTA traces in Fig. 3 show the largest exothermic peak for the matrix phenyl group combustion, and the corresponding peak positions are in agreement with the DTG signals. These thermoanalytic data are evidence for the encapsulation of the metal nanoparticles in the sol–gel materials. Clear differences in the DTG/TG and DTA traces are observed for the gels with and without metals. The most interesting effect is a reduction of the combustion temperature of matrix phenyl groups, when silver is encapsulated. This indicates that the encapsulated silver particles promote the combustion of the matrix phenyl groups.

Fig. 4 shows the influence of synthesis pH value and Au loading on the N_2 physisorption data. The analysis of the pore structure by BJH, and *t*-plot methods are listed in Table 1. Sample A is made at pH = 7, whereas samples B and C are made at pH = 6, but the latter two differ in metal loading. The Au loadings of samples A and B are similar, and they only differ in their synthesis pH value. The as-made sample A shows a type IV adsorption isotherm with a type H2 hysteresis. Such adsorption isotherms are observed for amorphous, mesoporous materials with a large variation of pore diameters. As the Au NPs are encapsulated inside the sol–gel material (see below), the mesoporous structure of the matrix allows for migration and sintering of the metal particles upon calcination, as already argued above for the growth of particles. The diameter of the mesopores is 3.9 nm from BJH analysis. Further analysis with the *t*-plot method yields a mesopore area of 396 $m^2 g^{-1}$, a mesopore volume

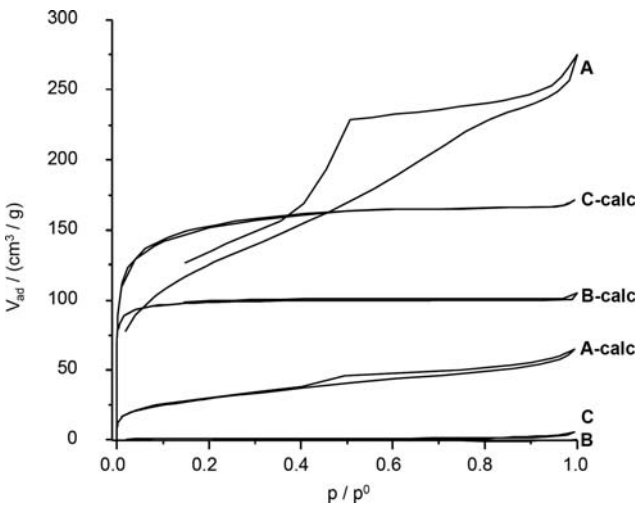

Fig. 4 N_2 adsorption isotherms of gold samples before and after calcination at 873 K: (A) Au/Si = 0.012, synthesized at pH = 7; (B) Au/Si = 0.014, pH = 6 and (C) Au/Si = 0.035, pH = 6.

View Article Online

Open Access Article. Published on 13 April 2010. Downloaded on 7/19/2025 5:50:03 AM.

Table 1 Surface area, pore volume and pore sizes of calcined materials. The BET surface area is placed in parentheses, when the *C* value is negative. This is most often observed for microporous materials, where the BET model is not reasonable

Sample	BET/m^2 g^{-1}	*t*-Plot: micropore volume/cm^3 g^{-1}; external surface area/m^2 g^{-1}; micropore area/m^2 g^{-1}	*t*-Plot: mesopore volume/cm^3 g^{-1}; external surface area/m^2 g^{-1}; mesopore area/m^2 g^{-1}	BJH_{des} pore diameter/nm
A	450 ± 2	—	0.30; 53.2; 396	3.9
A-calc	106.9 ± 0.3	—	0.05; 20.9; 86	3.5
B	0.10 ± 0.03	—	—	—
B-calc	325 ± 6	0.15; 0.3; 324	—	<1.9 and 2.5
C	3.99 ± 0.04	0.0017; 0.12; 3.87	—	<1.9
C-calc	518 ± 11	0.25; 3.5; 514	—	<1.8
D	0.86 ± 0.16	—	—	—
D-calc	462 ± 7	0.22; 7.4; 454	—	<2 and 3.5
D-calc after HNO_3	588.2 ± 1.9		0.39; 20.4; 567	3.9
F; (0)	188.5 ± 0.3	—	0.10; 47.4; 141	3.5
F-calc; (1)	361.3 ± 1.0	—	0.20; 27.7; 334	3.5
(1) After CO ox. + reduct.	207.8 ± 0.7	—	0.12; 38.2; 170	3.5
(2)	155.1 ± 1.1	—	0.10; 1.4; 154	3.4
(3)	305.6 ± 1.6	—	0.17; 31.0; 275	3.5
(4)	313.5 ± 2.1	—	0.18; 24.9; 289	3.5
G	561 ± 7	0.28; 10.9; 551		<1.8 and 3.5
G-calc	477 ± 3	0.22; 1.5; 476	—	<1.8 and 3.5
G-calc after HNO_3	344 ± 4	0.17; 3.6; 341	—	<1.9
H	0.55 ± 0.02	—	—	—
H-calc	424 ± 8	0.20; 1.4; 423	—	<2 and 3.9

of 0.30 cm^3 g^{-1}, and an external surface area of 53 m^2 g^{-1}. Sample A undergoes substantial shrinking upon calcination at 873 K with a reduced mesopore volume of 0.05 cm^3 g^{-1}, albeit the mesopore diameter remains almost constant at 3.5 nm. Obviously, the number of mesopores is reduced upon calcination, while their size is nearly unchanged. Reducing the synthesis pH value to 6 (sample B) induces a considerable change in the pore structure. The as-made gels with capped NPs are now dense, and only the calcined materials show microporosity with a remarkable micropore area of 324 m^2 g^{-1} for the Au sample with the lower loading, B-calc, and an even larger value of 514 m^2 g^{-1} for the higher loading, C-calc. It should be mentioned that a hybrid gel made at the same pH value without any metal loading shows some microporosity with a micropore area of 550 m^2 g^{-1} before calcination which shrinks to 476 m^2 g^{-1} after calcination. It can be concluded that the Au NPs modify the porosity of the material. We suggest that the Au NPs are encapsulated in the sol–gel material and calcination generates microporosity due to the removal of the NP capping agent and the matrix phenyl groups.

The strong influence of the synthesis pH value is also observed for the Ag samples. Fig. 5 shows the N_2 adsorption isotherms of the calcined samples for pH = 5 (sample H-calc), pH = 6 (sample D-calc) and pH = 7 (sample F-calc), and the pore analyses are listed in Table 1. Before calcination, samples D and H are dense, whereas sample F shows mesoporosity. At pH = 7, mesoporosity dominates the structure, also after calcination, and at pH = 5 micropores are observed after calcination. At pH = 6, a mixture of micro- and mesopores exists in sample D-calc. The inset in Fig. 5 shows the pore size analyses by the Barrett, Joyner and Halenda (BJH) method, confirming the mesoporous character of samples D and F with a pore diameter of 3.5 nm.

The trend in the pore structures of the materials raises the question of how this will affect the metal clusters' sintering behavior. We expect that the microporous materials will prevent the metal NPs from sintering, whereas the mesoporous materials

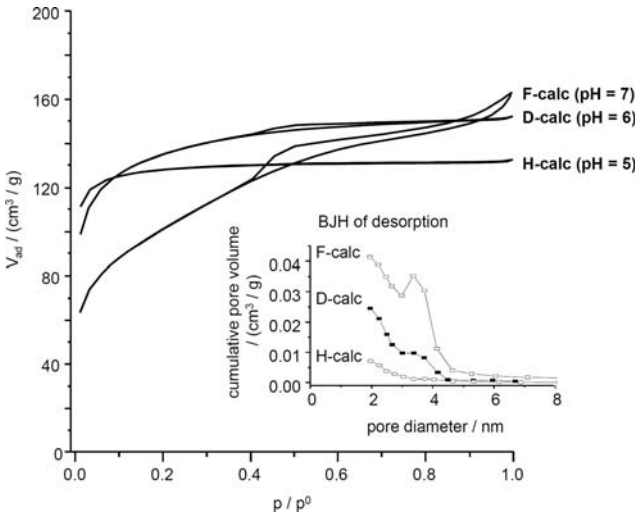

Fig. 5 Nitrogen sorption isotherms of calcined silver samples synthesized at different pH values. The metal loadings are Ag/Si = 0.033 for sample D, Ag/Si = 0.016 for sample F, and Ag/Si = 0.014 for sample H.

are likely to show particle aggregation at elevated temperatures. The TEM analysis in Fig. 6a confirms that the average particle size increases after calcination at 873 K. The highest particle size population before calcination exists at 6 nm with only few particles larger than 25 nm. In contrast, most particles are larger than 10 nm after calcination, although the loading is small (Ag/Si = 0.016). The TEM image of the calcined material also shows that metal particles exist outside the silica matrix, and some silver has sintered to short nanowires inside the pores of the matrix. (see inset with image negative in Fig. 6a). This sample was made at pH = 7, and it contains sufficiently large mesopores for the metal NPs to sinter in the pore structure of the matrix. A substantially different situation is observed for the material made

 This journal is © The Royal Society of Chemistry 2010

View Article Online

Open Access Article. Published on 13 April 2010. Downloaded on 7/19/2025 5:50:03 AM.

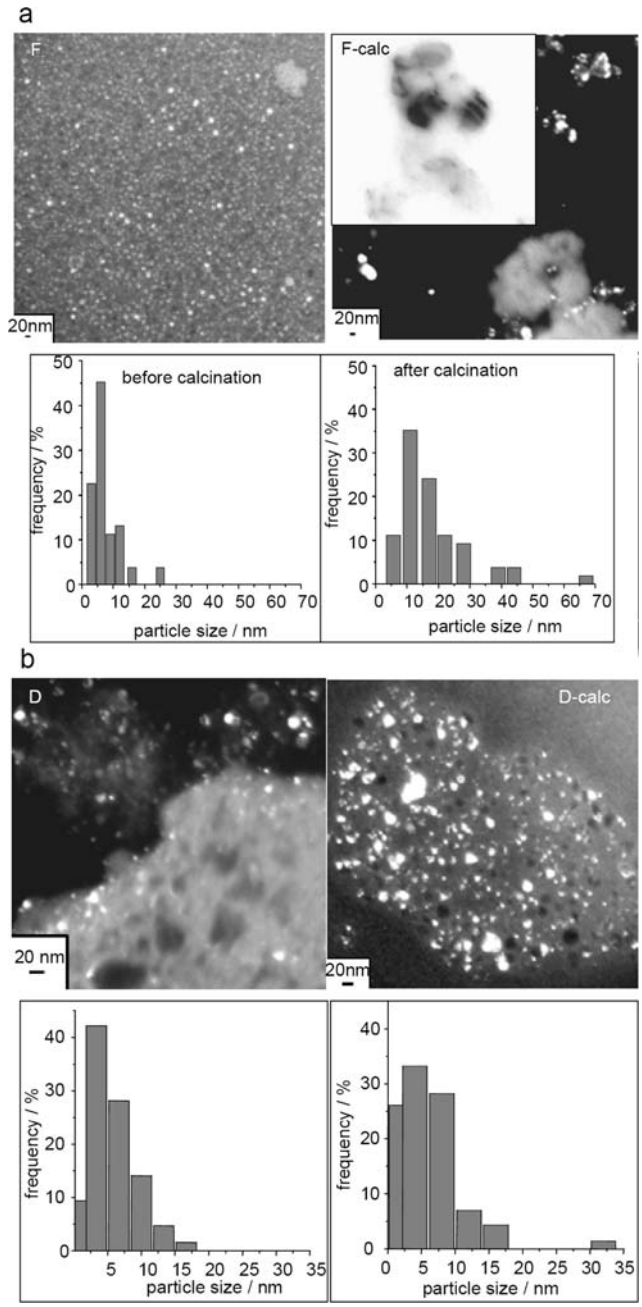

Fig. 6 Dark field images and particle size distribution of silica gels synthesized at (a) pH = 7, and (b) pH = 6 with silver (oxide) particles before and after calcination at 873 K.

at pH = 6 (Fig. 6b). The particle size distribution before and after calcination varies only slightly. Moreover, the majority of the NPs below 5 nm diameter are stable upon calcination. The loading, Ag/Si = 0.033, is even higher than for the sample shown in Fig. 6a.

The sintering behavior is another clear indication of the encapsulation of the NPs inside the sol–gel matrix. Final proof is obtained by the extraction of Ag NPs from the matrix by HNO_3 dissolution. The results of N_2 adsorption isotherms of the micro-/mesoporous sample before and after HNO_3 extraction are shown in Fig. S1 of the ESI†. The sample shows a brown color which converts to colorless after removal of the silver particles. The extracted sample shows mesopores with a much higher specific surface area than the microporous sample before Ag extraction. A blank experiment for a gel with the same matrix composition but without Ag shows that the generated pore space in the Ag sample can not originate from matrix erosion, and it must be assigned to pore space generated by the Ag NPs. XPS analyses indicate that the Ag particles were completely removed by HNO_3 extraction. Mesopores are expected upon removal of particles with an average diameter of 8 nm in this sample. The pore space generated by HNO_3 extraction is larger than expected by a factor of ~8 for the stoichiometric silver content. This indicates that matrix corrosion occurs in addition to the dissolution of the silver particles.

Fig. 7 shows the results of temperature programmed reduction (TPR) measurements carried out on silver samples that were prepared by different synthetic methods. All samples were calcined at 873 K prior to the TPR experiment. For comparison, the XRD powder diffraction patterns show the existence of different crystalline Ag phases. The silver oxide obtained after calcination of the sample F shows a peak at 500 K indicating reduction of the silver oxide. For comparison, a metal-free hybrid gel with the same matrix composition was post-synthetically impregnated with Ag NPs (sample I). The TPR reduction peak shifts to considerably higher temperatures with a maximum at 595 K. The XRD pattern shows that a mixture of both, silver oxides and metallic silver, exists in this sample. The higher TPR temperature indicates that the particles are larger than for the *in situ* encapsulated sample, F-calc. The third test (sample J) was carried out without the hybrid component, PhTS, in the sol–gel process, but the NPs were added as in the first sample. The reduction peak appears in the similar temperature range, but some broadening is observed and the peak has a lower intensity as in sample F. In addition, a reduction signal seems to appear at much higher temperatures above 600 K. This observation may indicate a large size distribution with contributions of much larger particles. Sample K-calc was made without capping agent, phenylethylthiol, and it shows no reduction signal. This is due to the fact that no silver oxide is observed in the XRD experiment. This sample only contains metallic silver. This set of experiments suggests that the use of phenylethylthiol in conjunction with the hybrid precursor composition with PhTS is important to stabilize

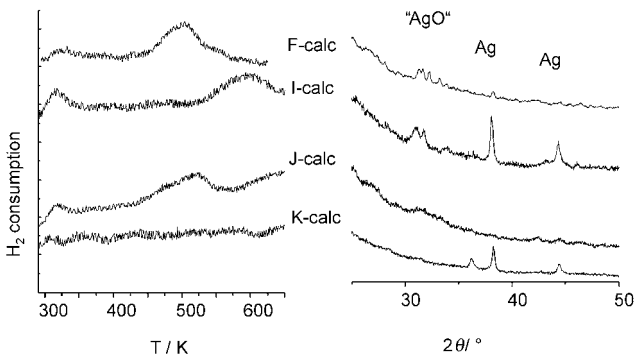

Fig. 7 TPR measurements and XRD patterns of samples with similar silver concentrations, but different synthesis procedures after calcination at 873 K.

View Article Online

Open Access Article. Published on 13 April 2010. Downloaded on 7/19/2025 5:50:03 AM.

silver with a small particle size. Oxidation of the small NPs occurs upon calcination, making them visible in the TPR experiment.

The matrix stability under the stress of calcination and reduction or catalytic test reactions of sample F was investigated by nitrogen adsorption. Further information can be found in Fig. S2 of the ESI†. These sample treatments and pore analyses show that the material is thermally and chemically stable. The pores do not collapse upon calcination, reduction or catalysis.

For the catalytic tests, we chose the simple oxidation of CO to CO_2 as a model reaction. Fig. 8 shows the performance of sample C-calc and of its silver analog (D-calc) in the catalytic oxidation of CO. The data for 0.05 mmol g^{-1} Au and Ag supported on alumina are added for comparison. A series of separate control experiments confirmed that plain SiO_2 and Al_2O_3 were inactive below 823 K. The data show that the materials are indeed catalytically active, even though they do not perform as well as the "state of the art" Ag- and Au-based CO oxidation catalysts.[13,38–40] After catalytic testing at 873 K, the supported Au and Ag catalysts showed clear metal deposits at the reactor exit, due to metal evaporation (see photos in Fig. 8). Such deposits were not observed for our "entrapped clusters" catalysts. The conversion on the embedded silver catalyst in our sol–gel material is the best among all tested materials. The metal must be redox active for the catalytic performance. From TPR data, silver fulfills this requirement much better and the particles are smaller than for the gold sample. This is most likely the reason for the better catalytic conversion on the silver catalyst.

Fig. 9 shows additional TPR investigations for silver samples which were made at different pH values. Sample F-calc before and after CO oxidation is mesoporous (synthesis at pH = 7) and the two TPR experiments clearly show that the metal particles are not stable in the catalytic oxidation and subsequent calcination: the TPR signal disappears after this treatment. In contrast, the sample D-calc which is micro-/mesoporous (synthesis at pH = 6) shows a remarkable stability in TPR.

Two competitive processes during the sol–gel process are most likely responsible for the observations: the assembly of the bare

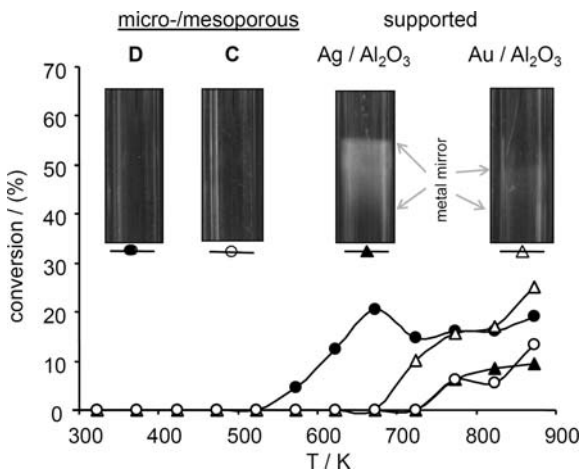

Fig. 8 CO oxidation with gold and silver catalysts; samples C and D are encapsulated metal catalysts and the two other samples are conventional supported catalysts for comparison; photos of the reactor exits after the catalytic test show metallic deposits for the supported catalysts only.

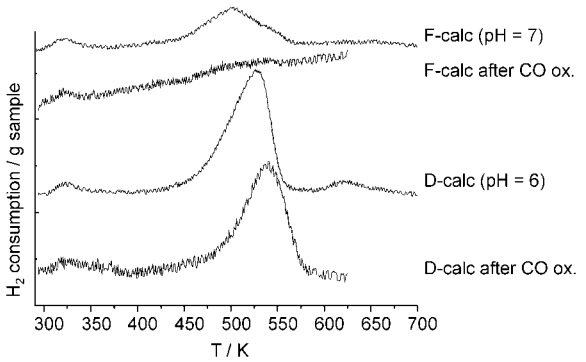

Fig. 9 TPR of calcined gels with encapsulated silver particles synthesized at different pH values.

metal nanoparticles with phenylethylthiol capping agent and the encapsulation of capped NPs in the sol–gel matrix. At high loadings, the self-assembly of bare NPs is strong, leading to phase separation of crystalline metal NPs. At lower loadings, the particles are encapsulated in the sol–gel matrix, although a growth of their size can be discerned after the sol–gel synthesis. This particle growth is more pronounced for gold than for silver, especially for the matrix that contains mesopores. Particle growth upon calcination is mainly influenced by the matrix porosity which is a function of synthesis pH value. While sintering is observed for mesoporous gels (synthesis pH = 7), this can be substantially suppressed for the microporous samples (pH = 6 and pH = 5).

Conclusions

Gold and silver nanoparticles were successfully encapsulated in organically modified silica gels in the sol–gel synthesis. Loadings of up to 6.6% (w/w) for gold and up to 3.7% (w/w) for silver were achieved without phase separation. The noble metal NPs clearly show a porogenic effect on the sol–gel system. A growth of the metal particles is discerned in the sol–gel process, and this is more pronounced for gold. Dissolving Ag with HNO_3 generates mesopores that were occupied by the metal NPs. Micropores are formed at synthesis pH values of 5–6, and mesopores are observed at pH = 7. The micropores are at least thermally stable up to 873 K.

Silver oxide is formed upon calcination of the materials which is due to the small size of the particles. The size of the metal NPs depends on the synthetic route, and the smallest particles are obtained using phenyltriethoxysilane as precursor of the hybrid gel. This is due to the optimized dispersion of the NPs which are able to interact *via* their capping agent, phenylethylthiol, with the phenyl groups of the matrix. The matrix porosity is retained under thermal and/or catalytic stress. The materials are catalytically active in CO oxidation, although relatively high activation temperatures of at least 600 K are needed. The NPs remain encapsulated in the sol–gel matrix after the catalytic reaction. The accessibility and the size of the NPs still offer room for optimization. With catalysts prepared at higher pH values, the NPs are too large for catalytic activity, although the pores are large enough for sufficient mass transport. At lower synthesis pH values, the particles are smaller and potentially able to catalyze

 This journal is © The Royal Society of Chemistry 2010

View Article Online

oxidation reactions. However, the microporous nature of the materials may hinder diffusion to the active sites. All that said, we feel that the non-covalent capping and encapsulating approach opens exciting opportunities for metal cluster catalysis.

Acknowledgements

We thank Dr D. Baither, Institute of Material Physics, WWU Münster for assistance with TEM micrographs, Dr M. C. Mittelmeijer–Hazeleger for carrying out one of the N_2 adsorption measurements, Dr A. V. Gaikwad for assistance in the synthesis of the Au and Ag nanoparticles, the Deutsche Forschungsgemeinschaft (DFG) and the Netherlands Organisation for Scientific Research (NWO) for financial support of the IRTG 1444 network.

References

1 U. Schubert, *J. Chem. Soc., Dalton Trans.*, 1996, 3343–3348.
2 R. J. P. Corriu and D. Leclercq, *Angew. Chem., Int. Ed. Engl.*, 1996, **35**, 1420–1436.
3 C. Sanchez, B. Julian, P. Belleville and M. Popall, *J. Mater. Chem.*, 2005, **15**, 3559–3592.
4 M. E. Davis, A. Katz and W. R. Ahmad, *Chem. Mater.*, 1996, **8**, 1820–1839.
5 M. Hunnius, A. Rufinska and W. F. Maier, *Microporous Mesoporous Mater.*, 1999, **29**, 389–403.
6 L. Pauling, *Chem. Eng. News*, 1949, **27**, 913.
7 G. Wulff and A. Sarhan, *Angew. Chem., Int. Ed.*, 1972, **11**, 341.
8 M. E. Davis, *Nature*, 2002, **417**, 813–821.
9 A. Corma and M. E. Davis, *ChemPhysChem*, 2004, **5**, 304–313.
10 Y. Yan and O. Ramström, *Molecularly Imprinted Materials, Science and Technology*, Marcel Dekker, New York, 2005.
11 J. D. Epping and B. F. Chmelka, *Curr. Opin. Colloid Interface Sci.*, 2006, **11**, 81–117.
12 E. L. Margelefsky, R. K. Zeidan and M. E. Davis, *Chem. Soc. Rev.*, 2008, **37**, 1118–1126.
13 G. Budroni and A. Corma, *Angew. Chem., Int. Ed.*, 2006, **45**, 3328–3331.
14 S. H. Joo, J. Y. Park, C. K. Tsung, Y. Yamada, P. D. Yang and G. A. Somorjai, *Nat. Mater.*, 2009, **8**, 126–131.
15 C. H. Bartholomew, *Appl. Catal., A*, 2001, **212**, 17–60.
16 P. Forzatti and L. Lietti, *Catal. Today*, 1999, **52**, 165–181.
17 L. M. van der Zande, E. A. de Graaf and G. Rothenberg, *Adv. Synth. Catal.*, 2002, **344**, 884–889.
18 G. Rothenberg, E. A. de Graaf and A. Bliek, *Angew. Chem., Int. Ed.*, 2003, **42**, 3366–3368.
19 L. Armelao, D. Barreca, G. Bottaro, A. Gasparotto, S. Gross, C. Maragno and E. Tondello, *Coord. Chem. Rev.*, 2006, **250**, 1294–1314.
20 E. Sacaliuc, A. M. Beale, B. M. Weckhuysen and T. A. Nijhuis, *J. Catal.*, 2007, **248**, 235–248.
21 J. Zhu, Z. Konya, V. F. Puntes, I. Kiricsi, C. X. Miao, J. W. Ager, A. P. Alivisatos and G. A. Somorjai, *Langmuir*, 2003, **19**, 4396–4401.
22 Z. Konya, V. F. Puntes, I. Kiricsi, J. Zhu, A. P. Alivisatos and G. A. Somorjai, *Nano Lett.*, 2002, **2**, 907–910.
23 T. Mokari, H. Sertchook, A. Aharoni, Y. Ebenstein, D. Avnir and U. Banin, *Chem. Mater.*, 2005, **17**, 258–263.
24 H. Bonnemann, U. Endruschat, B. Tesche, A. Rufinska, C. W. Lehmann, F. E. Wagner, G. Filoti, V. Parvulescu and V. I. Parvulescu, *Eur. J. Inorg. Chem.*, 2000, 819–822.
25 Y. W. Xie, S. Quinlivan and T. Asefa, *J. Phys. Chem. C*, 2008, **112**, 9996–10003.
26 S. R. Hall, S. A. Davis and S. Mann, *Langmuir*, 2000, **16**, 1454–1456.
27 G. Paul, S. Steuernagel and H. Koller, *Chem. Commun.*, 2007, 5194–5196.
28 S. Tsuzuki, K. Honda and R. Azumi, *J. Am. Chem. Soc.*, 2002, **124**, 12200–12209.
29 S. Tsuzuki, T. Uchimaru and M. Mikami, *J. Phys. Chem. A*, 2006, **110**, 2027–2033.
30 J. Sefcik and S. E. Rankin, *J. Phys. Chem. B*, 2003, **107**, 52–60.
31 C. J. Brinker and G. W. Scherer, *Sol–Gel Science, The Physics and Chemistry of Sol–Gel Processing*, Academic Press, San Diego, 1990.
32 M. Brust, M. Walker, D. Bethell, D. J. Schiffrin and R. Whyman, *J. Chem. Soc., Chem. Commun.*, 1994, 801–802.
33 R. Guo, Y. Song, G. L. Wang and R. W. Murray, *J. Am. Chem. Soc.*, 2005, **127**, 2752–2757.
34 S. W. Chen and R. W. Murray, *Langmuir*, 1999, **15**, 682–689.
35 M. M. Oliveira, D. Ugarte, D. Zanchet and A. J. G. Zarbin, *J. Colloid Interface Sci.*, 2005, **292**, 429–435.
36 G. Paul, J. Heimink and H. Koller, *Chem. Mater.*, 2008, **20**, 5083–5089.
37 A. Bögershausen, S. J. Pas, A. J. Hill and H. Koller, *Chem. Mater.*, 2006, **18**, 664–672.
38 M. C. Kung, R. J. Davis and H. H. Kung, *J. Phys. Chem. C*, 2007, **111**, 11767–11775.
39 H. Y. Liu, D. Ma, R. A. Blackley, W. Z. Zhou and X. H. Bao, *Chem. Commun.*, 2008, 2677–2679.
40 Y. S. Chi, H. P. Lin and C. Y. Mou, *Appl. Catal., A*, 2005, **284**, 199–206.

Open Access Article. Published on 13 April 2010. Downloaded on 7/19/2025 5:50:03 AM.